https://doi.org/10.5194/egusphere-2026-3573
Preprint. Discussion started: 20 July 2026

Dust-driven changes in particle pH differentially regulate secondary inorganic aerosol formation in central China

Hongyu Zhang[1, 2], Yating Zhang[1, 2], Yang Xiao[1, 2], Xiaohui Bi[1, 2]*, Shenbo Wang[3]*, Qili Dai[1, 2], Yinchang Feng[1, 2]

[1] Key Laboratory of Urban Air Particulate Pollution Prevention and Control of Ministry of Ecology and Environment, College of Environmental Science and Engineering, Nankai University, Tianjin 300350, China

[2] CMA-NKU Cooperative Laboratory for Atmospheric Environment-Health Research, Tianjin 300350, China

[3] Research Institute of Environmental Sciences, Zhengzhou University, Zhengzhou 450000, China

* Corresponding authors: Xiaohui Bi and Shenbo Wang

E-mail address: bixh@nankai.edu.cn and shbwang@zzu.edu.cn

https://doi.org/10.5194/egusphere-2026-3573
Preprint. Discussion started: 20 July 2026

Abstract

Dust episodes facilitate the long-range transport of crustal materials (CM), thereby increasing their contribution to particulate matter and influencing secondary inorganic aerosol (SNA) formation through changes in particle acidity. However, variations in precursor emissions, meteorological conditions, and particle acidity along dust transport pathways may cause the effects of dust input on SNA formation to differ among cities. Such intercity variability during the same regional dust episode remains insufficiently investigated. To address this gap, synchronous observations were conducted in seven cities in central China during a regional dust episode in April 2023. The results showed that, across the seven cities, the mean contribution of CM to $PM_{2.5}$ increased from 22.6% on clean days to 53.2% on dust days. Correspondingly, particle pH generally increased to 4.24–4.94 during the dust episode, mainly driven by non-volatile cations such as Ca^{2+} and Mg^{2+}. Calculations of aqueous-phase sulfate formation rates indicated that transition metal ion (TMI) catalyzed oxidation consistently dominated sulfate formation. However, this pathway was generally suppressed during the dust episode as particle pH increased. Although the O_3 and NO_2 oxidation pathways were enhanced, their increases could not offset the decrease in the TMI-catalyzed pathway. In contrast, elevated particle pH promoted nitrate partitioning. In cities with relatively low clean-day pH values within the rapid-response range of $\varepsilon(NO_3^-)$, even a non-maximum dust-induced pH increase could result in a pronounced increase in particulate nitrate. Therefore, future nitrate pollution control should consider the coordinated management of NO_x emissions and fugitive dust sources.

Keywords: $PM_{2.5}$; Crustal materials; Secondary inorganic aerosol; Particle acidity

https://doi.org/10.5194/egusphere-2026-3573
Preprint. Discussion started: 20 July 2026

Synopsis: Dust-derived crustal materials elevated particle pH, suppressing sulfate formation but promoting particulate nitrate partitioning during a regional dust episode.

Graphical abstract:

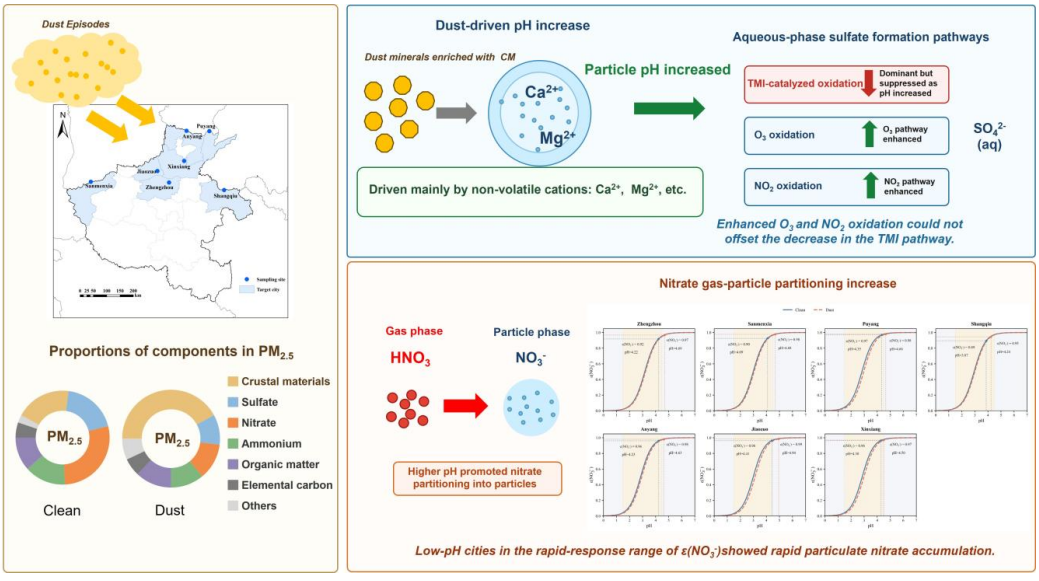

Highlights:

- Dust input made crustal materials the dominant $PM_{2.5}$ component;
- Non-volatile cations substantially elevated particle pH during the dust episode;
- Elevated particle pH suppressed TMI-catalyzed sulfate formation but promoted nitrate partitioning into the particle phase.

https://doi.org/10.5194/egusphere-2026-3573
Preprint. Discussion started: 20 July 2026

1 Introduction

Crustal materials (CM), mainly composed of elements or ions such as Si, Fe, Al, Ca, Mg, and Na, are important components of atmospheric particulate matter (Després et al., 2012). CM are widely present in the atmosphere, with particle sizes ranging from less than 0.1 μm to more than 100 μm, spanning over three orders of magnitude (Mahowald et al., 2014; Ryder et al., 2019). Globally, the annual emission of CM is second only to sea salt, at approximately 1840 Tg yr^{-1}. The atmospheric burden of CM is about 19.2 Tg, accounting for more than two-thirds of the global aerosol mass (Textor et al., 2006).

CM originate from both anthropogenic and natural sources. Anthropogenic CM are mainly derived from fugitive dust generated by human activities, such as road dust and construction dust (Wu et al., 2020; Chen et al., 2023). Natural CM are mainly associated with dust transport and wind-driven resuspension of exposed surfaces or soils (McKendry et al., 2007; Chen et al., 2018). As an important source of CM, dust episodes can transport large amounts of crustal materials and rapidly increase particulate matter concentrations in downwind cities (Chen et al., 2024). The North China Plain is frequently affected by dust episodes under the influence of synoptic systems such as Mongolian cyclones and cold high-pressure systems, making dust transport an important input of crustal materials into atmospheric particulate matter (Chen et al., 2023; Huo et al., 2025). During dust episodes, coarse particle concentrations can increase to 1.39–19.7 times the pre-dust levels, with maximum concentrations reaching 3076 μg/m^3. Meanwhile, CM concentrations in $PM_{2.5}$ may increase to 54.0 μg/m^3, contributing up to 71.8% of $PM_{2.5}$ mass (Dong et al., 2020; Wei et al., 2022; Zhang et al., 2025).

https://doi.org/10.5194/egusphere-2026-3573
Preprint. Discussion started: 20 July 2026

Secondary inorganic aerosols (SNA), consisting of SO_4^{2-}, NO_3^-, and NH_4^+, are major components of $PM_{2.5}$. In eastern China, their contribution can exceed 50% (Wei et al., 2023) and can further increase to 67% during pollution episodes (Wang et al., 2023). SO_4^{2-} is mainly formed through SO_2 oxidation (Tao et al., 2020). In the gas phase, SO_2 can be oxidized by •OH to form H_2SO_4, which subsequently partitions into the particle phase (Song et al., 2021; Wang et al., 2022). In the aqueous phase, SO_2 dissolves into aerosol water to form S(IV), which is further oxidized to SO_4^{2-} by H_2O_2, O_3, NO_2, and transition metals such as Fe and Mn (Tao et al., 2020; Wang et al., 2022). During the daytime, nitrate is mainly formed through the reaction of NO_2 with •OH to produce HNO_3, followed by partitioning into the particle phase (Liu et al., 2025; Nenes et al., 2020). At night, NO_2 is first oxidized by O_3 to form $NO_3^•$, which further reacts with NO_2 to produce N_2O_5 (Yan et al., 2019; Ma et al., 2023). Subsequent heterogeneous hydrolysis of N_2O_5 leads to nitrate formation (Nenes et al., 2020; Zhao et al., 2023). Aerosol pH is a key factor regulating SNA formation. For sulfate, pH can alter the aqueous-phase speciation of S(IV), thereby regulating the relative contributions of different sulfate formation pathways (Pye et al., 2020; Tilgner et al., 2021). For nitrate, its strong semi-volatility makes gas-particle partitioning highly sensitive to aerosol pH (Zhou et al., 2022). Dust-derived CM, including non-volatile cations such as Ca^{2+}, Mg^{2+}, and Na^+, as well as elements such as Ca, Al, and Fe, can neutralize particle acidity, increase aerosol pH, and further affect aerosol liquid water content, thereby influencing SNA formation (Karydis et al., 2021; Itahashi et al., 2022; Lang et al., 2025). In addition, the large specific surface area of mineral particles provides heterogeneous reaction interfaces for precursors such as SO_2 and NO_2 (Jia et al., 2021; Liu et al., 2022; Li et al., 2025). Transition metals such as Fe and Mn can participate in oxidation reactions and promote sulfate formation (Wang et al.,

https://doi.org/10.5194/egusphere-2026-3573
Preprint. Discussion started: 20 July 2026

2021; Zhang et al., 2024). CM can heterogeneously react with NO_2 and take up gaseous HNO_3, leading to particulate nitrate formation through surface reactions and acid–base neutralization (Jia et al., 2021; Hrdina et al., 2021; Milousis et al., 2025). Lang et al. (2025) found that the input of abundant non-volatile cations during dust episodes enhanced the buffering capacity of particle acidity and reduced the dependence of nitrate formation on NH_3, thereby weakening the effect of NH_3 emission reduction on nitrate formation to some extent. These findings suggest that SNA formation mechanisms may change substantially during dust episodes. However, as dust plumes pass through different cities, SO_2, NO_x, and NH_3 emissions, meteorological conditions, and particle acidity can vary considerably. The effects of dust input on SNA formation may therefore differ among cities, but this issue remains insufficiently investigated.

Central China is frequently affected by dust transported from northern source regions toward the North China Plain and central-eastern China (Tang et al., 2020; Zhang et al., 2024). In spring, enhanced Mongolian cyclones, cold high-pressure systems, and cold frontal activities can transport dust southeastward from the Mongolian Plateau and affect the region (Chen et al., 2023; Borjigin et al., 2024; Huo et al., 2025). Multiple dust transport events have also been observed in this region in spring, autumn, and winter (Dong et al., 2020; Tang et al., 2020; Huo et al., 2025). Meanwhile, SNA are the dominant components of $PM_{2.5}$ in this region, contributing 53%–63% of $PM_{2.5}$ mass and increasing to 67% during heavy pollution episodes (Wang et al., 2022, 2023). Previous studies further showed that particle pH in this region is jointly affected by TNH_x and non-volatile cations, indicating that local SNA formation and gas-particle partitioning are sensitive to the aerosol acid-base environment (Wang et al., 2020).

https://doi.org/10.5194/egusphere-2026-3573
Preprint. Discussion started: 20 July 2026

In this study, observational data collected synchronously across seven cities in an urban agglomeration in central China agglomeration during April 2023 were analyzed. We compared $PM_{2.5}$ chemical composition between clean and dust days, explored the causes of intercity differences in particle pH under these two conditions, and analyzed the effects of dust episodes on sulfate formation rates and nitrate gas-particle partitioning. This study aims to clarify the impacts of dust input on particle acidity and SNA formation in central China, and to provide a scientific basis for the coordinated control of particulate nitrate and crustal materials.

2 Experiment and methods

2.1 Observation Sites

Online measurements of particulate matter and its chemical components were conducted in seven cities in Henan Province, China, from 7 to 17 April 2023. The observation sites included Zhengzhou (34.78° N, 113.81° E), Sanmenxia (34.80° N, 111.17° E), Puyang (36.20° N, 115.17° E), Shangqiu (34.57° N, 115.67° E), Anyang (36.21° N, 114.40° E), Jiaozuo (35.10° N, 113.42° E), and Xinxiang (35.38° N, 114.32° E). Descriptions and the spatial distribution of the seven observation sites in Henan Province are shown in Fig. S1 and Table S4.

2.2 Measurements

A Monitor for AeRosols and Gases in ambient Air (MARGA, Metrohm, Switzerland) was used to measure water-soluble inorganic ions (Na^+, NH_4^+, K^+, Mg^{2+}, Ca^{2+}, Cl^-, NO_3^-, and SO_4^{2-}) and gaseous species (NH_3, HCl, and HONO) at a 1 h time resolution. The MARGA system was also configured to

https://doi.org/10.5194/egusphere-2026-3573
Preprint. Discussion started: 20 July 2026

measure gaseous HNO_3 at all seven sites. However, HNO_3 concentrations were generally low during this campaign, resulting in small chromatographic peaks and relatively large uncertainties in peak integration. Previous MARGA evaluations have shown that low HNO_3 concentrations can increase relative variability and bias, while adsorption onto inlets and sampling tubing can further impair measurement accuracy (Rumsey et al., 2014; Rumsey and Walker, 2016; Chen et al., 2017). Consequently, gaseous HNO_3 measurements from all seven sites could not be quality assured and were excluded from the final dataset and subsequent quantitative analyses. Ambient air was introduced through a $PM_{2.5}$ inlet, after which particles and gases entered a wet rotating denuder for separation and dissolution. Particles were collected after hygroscopic growth and condensation in a steam-jet aerosol collector and were then analyzed by ion chromatography. Gaseous species were oxidized by H_2O_2 in the denuder, absorbed into the liquid solution, and subsequently quantified by ion chromatography (Rumsey et al., 2014; Trebs et al., 2004). Inorganic elements in $PM_{2.5}$ were measured using an energy-dispersive X-ray fluorescence analyzer (Xact 625, Cooper Environmental Services, USA) with a time resolution of 1 h. The measured elements included Na, Mg, Al, Si, P, S, Cl, K, Ca, Ti, V, Cr, Mn, Fe, Co, Ni, Cu, Zn, Ga, As, Se, Sr, Sn, Sb, Ba, and Pb. Ambient particles passed through a $PM_{2.5}$ inlet and were deposited on a Teflon filter tape. After approximately 1 h of sampling, the filter spot was moved to the analysis position, where elemental concentrations were determined by X-ray fluorescence and converted to mass concentrations using the instrument software. Organic carbon (OC) and elemental carbon (EC) were measured using a semi-continuous carbon analyzer (Model-4, Sunset Laboratory, USA). The measurement was based on the thermal–optical transmittance method following the NIOSH-5040 protocol. Carbon detected under a pure He atmosphere was defined as OC, while carbon

https://doi.org/10.5194/egusphere-2026-3573
Preprint. Discussion started: 20 July 2026

oxidized under a mixed atmosphere of 90% He and 10% O_2 was defined as EC.

$PM_{2.5}$, PM_{10}, and gaseous pollutants, including O_3, SO_2, and NO_2, were obtained from online analyzers (Thermo Electron, USA). Meteorological parameters, including wind speed (WS), temperature (T), relative humidity (RH), and pressure (P), were recorded simultaneously using an automatic weather station (LUFFT-WS500, Sutron Corporation, Germany). The accuracies were 0.1 m/s for WS, ±0.2 °C for T, ±2% for RH, and ±0.5 hPa for P. Detailed operating principles and quality assurance procedures are provided in Supplementary Text S1.

2.3 Data Analysis

2.3.1 Mass reconstruction

The calculation method for CM is as follows (Tian et al., 2016):

$$[CM]=1.89\times[Al] + 2.14\times[Si] + 1.4\times[Ca] + 1.43\times[Fe]+1.94[Ti] \quad (1)$$

where [Al], [Si], [Ca], [Fe], and [Ti] represent the concentrations of the respective elements (μg/m^3). As Ti was not available in the present dataset, the CM concentration was calculated using the measured concentrations of Al, Si, Ca, and Fe only.

2.3.2 Thermodynamic model

The particle pH was calculated using the ISORROPIA-II model (version 2.1, http://isorropia.eas.gatech.edu). The input data (excluding RH ≤ 30%), including SO_4^{2-}, TNO_3, TNH_x (NH_3+ NH_4^+), Ca^{2+}, K^+, Na^+, Mg^{2+}, Cl^-, RH and T. For the TNO_3 input, the measured particulate NO_3^- concentration was used directly at all seven sites, and no gaseous HNO_3 concentration was included.

https://doi.org/10.5194/egusphere-2026-3573
Preprint. Discussion started: 20 July 2026

As described in Sect. 2.2, the MARGA system was configured to measure gaseous HNO_3, but quality-assured HNO_3 data were unavailable because the ambient concentrations were generally low and the corresponding chromatographic peaks were subject to relatively large integration uncertainty. The concentrations of hydrogen ions in air (H^+_{air}) and ALWC were derived from the Na^+-K^+-Ca^{2+}-Mg^{2+}-NH_4^+-SO_4^{2-}-NO_3^--Cl^--H_2O equilibrium composition system. Activity coefficients for H^+ and OH^- were fixed at unity, while other ion pairs (e.g., H^+-Cl^-) employed the Kusik-Meissner parameterization for ionic activity calculations (Fountoukis and Nenes, 2007). pH values were calculated using the following formula:

$$pH = -\log_{10} H^+_{aq} \cong -\log_{10} \frac{1000 H^+_{air}}{ALWC_i + ALWC_o} \cong -\log_{10} \frac{1000 H^+_{air}}{ALWC_i} \quad (2)$$

$$ALWC_o = \frac{m_{org}\rho_w}{\rho_w} \frac{\kappa_{org}}{\left(\frac{1}{RH} - 1\right)} \quad (3)$$

where $ALWC_i$ and $ALWC_o$ refer to the ALWC for inorganic and organic components, respectively. m_{org} denotes the mass of organic aerosol, ρ_w is the density of water (1.0 g/cm^3), ρ_{org} is the density of organic material (1.4 g/cm^3) (Guo et al., 2015); k_{org} is the hygroscopicity parameter for organic aerosol (0.087) (Chang et al., 2010; Li et al., 2016). The ISORROPIA-II model operated under metastable conditions in the forward mode.

2.3.3 HYSPLIT analysis

Backward trajectories were calculated using the mixed-particle Lagrangian integrated trajectory method (HYSPLIT, https://www.ready.noaa.gov/HYSPLIT_traj.php). Meteorological input data were from the Global Data Assimilation System (GDAS) with 3D wind vectors, temperature, relative

https://doi.org/10.5194/egusphere-2026-3573
Preprint. Discussion started: 20 July 2026

humidity, geopotential height, surface pressure, and boundary layer diagnostics. 24-hour backward trajectories were simulated for air masses arriving at 500 m above ground level in each city, and trajectories from 11 to 13 April 2023 were further clustered to characterize the air-mass transport pathways during the dust pollution episode.

2.3.4 Calculation of aqueous-phase sulfate formation rates

Aqueous-phase SO_2 oxidation includes several pathways, such as oxidation by H_2O_2, O_3, and NO_2, transition metal ion (TMI)-catalyzed oxidation, methyl hydroperoxide oxidation, and peracetic acid oxidation (Zheng et al., 2015; Wang et al., 2021). Among TMIs, Ti(III), V(III), Cr(III), Co(II), Ni(II), Cu(II), and Zn(II) generally show relatively low catalytic activity. In addition, atmospheric concentrations of methyl hydroperoxide and peracetic acid are usually low. Therefore, only oxidation catalyzed by Fe(III) and Mn(II) was considered in this study. Because H_2O_2 measurements were not available, the H_2O_2 oxidation pathway was not calculated. The calculation methods for different oxidation pathways are summarized in Table S1, and the detailed equations and procedures are provided in Supplementary Text S2.

2.3.5 Calculation of nitrate gas-particle partitioning

Under conditions favorable for particulate nitrate formation, ambient HNO_3 concentrations are typically substantially lower than particulate NO_3^- concentrations (Ding et al., 2019). Previous thermodynamic studies have shown that when aerosol pH exceeds approximately 2.5–3.0, most inorganic nitrate resides in the particle phase, and $\varepsilon(NO_3^-)$ is comparatively insensitive to moderate pH variations (Vasilakos et al., 2018; Guo et al., 2018). The modeled particle pH values in this study were

https://doi.org/10.5194/egusphere-2026-3573
Preprint. Discussion started: 20 July 2026

generally above this threshold. Therefore, gaseous HNO_3 was expected to account for only a minor fraction of TNO_3, and its omission from the TNO_3 input was expected to have a limited influence on the estimated $\varepsilon(NO_3^-)$. According to the method proposed by Guo et al. (2016), the estimated nitrate partitioning ratio was calculated as follows:

$$\varepsilon(NO_3^-) = \frac{H_{HNO_3} \times K_{n1} \times ALWC \times RT(0.987 \times 10^{-14})}{\gamma_{NO_3^-} \cdot \gamma_{H^+} \times 10^{-pH} + H_{HNO_3} \times K_{n1} \times ALWC \times RT(0.987 \times 10^{-14})} \quad (4)$$

where H_{HNO_3} is the Henry's law constant of HNO_3, with units of atm^{-1}; K_{n1} is the dissociation constant of HNO_3, which depends on temperature, with units of $mol^2 \cdot kg^{-2}$; ALWC is the mean aerosol liquid water content derived from the ISORROPIA-II thermodynamic model using the measured water-soluble inorganic ions as input, with units of $\mu g/m^3$; R is the gas constant, with units of $J \cdot mol^{-1} \cdot K^{-1}$; T is the mean temperature during the observation period, with units of K; 0.987×10^{-14} is the unit conversion factor; and $\gamma_{NO_3^-} \cdot \gamma_{H^+}$ represents the activity coefficient product of NO_3^- and H^+, which is assumed to be 1.0 under ideal conditions. The product $H_{HNO_3} \times K_{n1}$ is the overall equilibrium constant based on the molar concentration of HNO_3. It was calculated using Eq. (40) reported by Clegg et al. (1998), with the unit conversion from atm^{-1} to $mol^2\ kg^{-2}\ atm^{-1}$ performed according to their Eq. (5).

3 Results and discussion

3.1 Identification and evolution of the regional dust episode

A relatively severe dust episode occurred across central China in April 2023. As shown in Fig. 1, the concentrations of PM_{10}, CM, and Ca^{2+} increased synchronously in Zhengzhou (ZZ), Sanmenxia (SMX), Puyang (PY), Shangqiu (SQ), Anyang (AY), Jiaozuo (JZ), and Xinxiang (XX) during the

https://doi.org/10.5194/egusphere-2026-3573
Preprint. Discussion started: 20 July 2026

observation period, with two peaks observed from 11 to 13 April and from 14 to 16 April. The backward trajectories on 13 April (Fig. S2) showed that all seven cities were influenced by air masses transported from the northwest. These air masses originated from Mongolia, Inner Mongolia, and northwestern dust source regions, and were transported to Henan through the North China region, indicating that this episode was closely related to the long-range transport of dust-laden air masses from the northwest. During this period, PM_{10} concentrations in all seven cities increased to more than twice their pre-dust levels. AY and PY were the most strongly affected by dust transport, with PM_{10} concentrations increasing by factors of 4.7 and 4.1, respectively. The mean CM concentrations on dust days also varied substantially among cities. During the dust episode, ZZ exhibited the highest concentration of CM in $PM_{2.5}$ (65.8 ± 34.3 μg/m^3), followed by AY (48.7 ± 27.3 μg/m^3) and JZ (44.8 ± 26.3 μg/m^3), whereas XX had the lowest concentration (18.3 ± 10.6 μg/m^3). Although ZZ was located downstream of the dust transport pathway, it exhibited the highest CM concentration and a relatively long pollution duration. This may be attributed to the dominance of moderate and low wind speeds during the dust episode, which was unfavorable for dust dispersion and may have also facilitated the resuspension of local fugitive dust. Therefore, although this dust episode showed a clear regional transport signal, the increases in PM_{10}, CM, and Ca^{2+} concentrations, as well as the duration of their peaks, differed among cities. This suggests that atmospheric particles and their chemical components were still affected by local emissions during dust transport. During the second peak, wind speeds were generally lower than those during the main dust period, accompanied by lower relative humidity and higher temperature (Figs. S3 and S4). This peak was likely associated with the combined effects of regional dust retention and local fugitive dust resuspension.

https://doi.org/10.5194/egusphere-2026-3573
Preprint. Discussion started: 20 July 2026

3.2 Changes in $PM_{2.5}$ chemical composition during the dust episode

Figure 2 shows the mass concentrations and fractional contributions of reconstructed $PM_{2.5}$ components in ZZ, SMX, PY, SQ, AY, JZ, and XX. On clean days, $PM_{2.5}$ composition in these cities was strongly influenced by secondary formation, with secondary inorganic aerosols (SNA, including SO_4^{2-}, NO_3^-, and NH_4^+) representing the major component in most cities. Except for ZZ (39.1%) and SMX (36.4%), the SNA contribution exceeded 40% in the other five cities, and reached 57.4%, 50.5%, and 53.9% in XX, AY, and PY, respectively. This pattern is generally consistent with previous studies (Dong et al., 2020; Wang et al., 2022). Notably, CM already accounted for a considerable fraction of $PM_{2.5}$ on clean days. Its contribution exceeded 20% in all cities and was higher than 30% in ZZ and SMX, indicating that crustal materials remained an important component of regional $PM_{2.5}$ even outside dust periods.

During the dust episode, both the concentration and fractional contribution of CM increased rapidly, making CM the dominant component of $PM_{2.5}$ in all cities. The largest increases in CM concentration were observed in PY and AY, where the mean concentrations increased from 3.9 ± 1.6 and 8.8 ± 3.2 μg/m^3 on clean days to 25.8 ± 15.3 and 48.7 ± 27.3 μg/m^3 on dust days, respectively, corresponding to increases by factors of 5.6 and 4.5. The average CM contribution across the seven cities increased from 22.6% on clean days to 53.2% on dust days, corresponding to a 2.4-fold increase. ZZ showed the highest CM contribution on dust days, reaching 68.1%, about twice that on clean days. The CM contributions in AY and JZ increased to 62.2% and 58.2%, respectively, both corresponding to approximately 2.7-fold increases. Although the CM contributions in PY and XX were lower than those in ZZ, AY, and JZ on dust days, their increases were more pronounced because of their relatively

https://doi.org/10.5194/egusphere-2026-3573
Preprint. Discussion started: 20 July 2026

low clean-day levels, reaching 3.8 and 3.2 times the clean-day values, respectively. Ca^{2+} also showed a clear response to dust input. The most pronounced increases in Ca^{2+} concentration occurred in PY, SQ, and AY, where concentrations increased from 0.7 ± 0.2, 0.5 ± 0.2, and 0.8 ± 0.2 μg/m^3 on clean days to 3.3 ± 2.3, 2.3 ± 2.1, and 3.5 ± 1.8 μg/m^3 on dust days, respectively, increasing by factors of 3.8, 3.6, and 3.5. The fractional contribution of Ca^{2+} to $PM_{2.5}$ also increased markedly during the dust episode. The increases were more evident in SQ and PY, where the Ca^{2+} contribution increased from 1.3% and 1.9% to 3.8% and 5.4%, respectively, representing increases of approximately 1.9 and 1.8 times the clean-day levels. The Ca^{2+} contributions in XX and AY increased moderately by factors of approximately 1.5 and 1.3, respectively. In contrast, SMX showed the weakest increase, with only an approximately 0.5-fold increase in Ca^{2+} contribution. These results suggest that the response of the Ca^{2+} contribution to dust input differed among cities.

In addition to CM and Ca^{2+}, the mean concentrations of OM, Na^+, and Mg^{2+} also increased on dust days. However, their fractional contributions to $PM_{2.5}$ did not increase accordingly because of the rapid increase in CM. For example, OM concentrations in PY and AY increased from 8.9 and 6.3 μg/m^3 on clean days to 11.3 and 8.3 μg/m^3 on dust days, whereas their contributions decreased from 25.2% and 16.4% to 18.6% and 10.7%, respectively. EC concentrations changed only slightly, and their contributions decreased in all cities. The largest decreases occurred in AY and SQ, where EC contributions declined from 3.4% and 2.9% on clean days to 1.5% and 1.4% on dust days, respectively. Although the rapid increase in crustal materials reduced the fractional contribution of SNA on dust days, SNA concentrations remained relatively high. For example, SNA concentrations reached 14.2 μg/m^3 in PY and 14.1 μg/m^3 in SQ. Among the three SNA components, NO_3^- remained the dominant

https://doi.org/10.5194/egusphere-2026-3573
Preprint. Discussion started: 20 July 2026

species on dust days. NO_3^- concentrations reached 6.4 μg/m^3 in PY and 6.3 μg/m^3 in SQ, both higher than the corresponding SO_4^{2-} and NH_4^+ concentrations. SO_4^{2-} also remained at relatively high levels during the dust episode, especially in SMX, SQ, and JZ, with concentrations of 4.6, 4.5, and 4.4 μg/m^3, respectively. The variations in SOR and NOR further support this interpretation (Figs. 3 and 4). On dust days, SOR values in SMX, PY, and ZZ were 0.36, 0.32, and 0.30, respectively, while NOR values in AY, ZZ, and XX were 0.56, 0.50, and 0.47, respectively. Although sulfur and nitrogen oxidation ratios decreased compared with clean days, they remained at relatively high levels, indicating that substantial nitrate and sulfate formation still occurred in central China during the dust episode.

3.3 Drivers of particle pH during the dust episode

Figure 5 shows the particle pH values calculated using the ISORROPIA-II model for seven cities in central China, under clean and dust conditions. During the dust episode, particle pH increased markedly in all cities under the influence of long-range dust transport. Except for XX, particle pH increased by more than 0.6 units in each city. JZ showed the largest increase, with particle pH rising from 4.19 to 4.94, corresponding to an increase of approximately 0.75 units. In contrast, XX was least affected by dust input, with particle pH increasing only from 4.05 to 4.50, by 0.45 units. This pattern is generally consistent with previous studies (Wang et al., 2020; Zhang et al., 2024). The increase in particle pH can be mainly attributed to the input of alkaline crustal materials during dust transport, which buffered acidic species in particles, thereby reducing particle acidity and increasing particle pH (Ding et al., 2019; Karydis et al., 2021). Notably, similar to clean days, substantial intercity differences in particle pH were still observed during the dust episode. The mean particle pH values on dust days

https://doi.org/10.5194/egusphere-2026-3573
Preprint. Discussion started: 20 July 2026

311 followed the order JZ (4.94) > ZZ (4.68) > PY (4.67) > SMX (4.66) > AY (4.65) > XX (4.50) > SQ
312 (4.24), indicating that particle acidity during the dust episode was still strongly influenced by local
313 emission characteristics.

314 To identify the main factors responsible for intercity differences in particle pH on clean days,
315 sensitivity analyses were performed for key influencing parameters. For each sensitivity test, the range
316 of a given parameter was input into the ISORROPIA-II model, while the other parameters were fixed
317 at their mean values. The corresponding particle pH was then calculated under different values of the
318 selected parameter. The sensitivity results showed that particle pH in all cities increased with
319 increasing concentrations of TNH_x, Ca^{2+}, Mg^{2+}, and other cations (Figs. S5, S6, and S8), but decreased
320 with increasing SO_4^{2-} concentration (Fig. S7). Notably, particle pH also showed an increasing trend
321 with increasing TNO_3 concentration in all cities (Fig. S9). This may be related to the overall low
322 concentrations of chemical components and relatively high levels of crustal cations on clean days.
323 Under such conditions, increased TNO_3 was more likely to combine with alkaline cations to form
324 nitrate salts, so that the H^+ concentration did not increase accordingly (Fig. S10), whereas aerosol
325 liquid water content (ALWC) increased (Fig. S11), leading to an increase in particle pH.

326 On clean days, when particles were mainly influenced by local conditions, JZ showed the highest
327 particle pH, with a value of 4.19. This was likely associated with its relatively high TNH_x concentration,
328 which averaged 32.7 μg/m^3 and was much higher than those in the other cities. In addition, Ca^{2+} and
329 Mg^{2+} concentrations in JZ were also relatively high, reaching 1.0 and 0.2 μg/m^3, respectively. Although
330 JZ had the highest SO_4^{2-} concentration among the seven cities, at 5.8 μg/m^3, its high TNH_x and Ca^{2+}
331 concentrations substantially neutralized acidic species, resulting in the lowest particle acidity among

https://doi.org/10.5194/egusphere-2026-3573
Preprint. Discussion started: 20 July 2026

the cities. In contrast, SQ had the lowest particle pH, with a value of only 3.58. This was mainly due to its relatively low TNH_x and Ca^{2+} concentrations, which were 21.1 and 0.5 μg/m^3, respectively, together with a high SO_4^{2-} concentration of 5.8 μg/m^3. These conditions led to insufficient buffering of particle acidity and made SQ the most acidic city among the seven sites. It is worth noting that SMX had the lowest TNH_x concentration among the seven cities, at only 17.5 μg/m^3, but its particle pH was 4.03, much higher than that in SQ. This was likely because SMX had the highest levels of crustal components among the seven cities, with Ca^{2+} and Mg^{2+} concentrations of 1.6 and 0.3 μg/m^3, respectively, which greatly enhanced the buffering capacity of particles. Meanwhile, its SO_4^{2-} concentration was the lowest among the seven cities, at only 4.8 μg/m^3, indicating relatively weak input of acidic components.

To quantify the contribution of individual factors to particle pH changes during the dust episode, a single-factor substitution method was applied. Specifically, one parameter under clean-day conditions was replaced by its corresponding dust-day value, while all other parameters were kept unchanged. The modified inputs were then used in the ISORROPIA-II model to calculate the resulting pH, and the contribution of each factor to ΔpH was obtained. As shown in Fig. 6, the increase in Ca^{2+} concentration was the key factor driving the rise in particle pH on dust days. Ca^{2+} can combine with SO_4^{2-} to form poorly soluble $CaSO_4$, which may precipitate from aerosol water, thereby reducing H^+ concentration and particle acidity (Ding et al., 2019; Karydis et al., 2021). In addition, increases in non-volatile cations such as Mg^{2+} and Na^+ during the dust episode further promoted the increase in particle pH, consistent with previous studies (Zhou et al., 2022; Lang et al., 2025). Besides non-volatile cations, the decrease in SO_4^{2-} concentration on dust days also reduced H^+ concentration and ALWC in

https://doi.org/10.5194/egusphere-2026-3573
Preprint. Discussion started: 20 July 2026

aerosol water, contributing to the increase in pH (Ding et al., 2019; Zhang et al., 2021). In contrast, increased relative humidity did not cause large changes in particle pH, whereas increased temperature led to a marked decrease in particle pH.

The contribution of Ca^{2+} to particle pH varied among cities. SMX and SQ were the most strongly affected by Ca^{2+} during the dust episode, with Ca^{2+} increasing particle pH by approximately 1.01 and 0.91 units, respectively. However, their particle pH values remained relatively low because of the suppressing effects of TNO_3 and temperature. Despite the marked pH increase associated with Ca^{2+} input, SQ still exhibited the lowest particle pH among the seven cities during the dust episode, owing to its relatively high initial acidity and limited buffering capacity under clean conditions. ZZ and PY were also markedly affected by Ca^{2+}, with particle pH increasing by 0.81 and 0.69 units, respectively. In addition, the decrease in SO_4^{2-} concentration was larger in ZZ and PY than in SMX and SQ, resulting in higher dust-day particle pH in ZZ and PY. Notably, in JZ, the effects of Ca^{2+} and SO_4^{2-} on dust-day pH were both weaker than those in ZZ, and the suppressing effect of TNO_3 was stronger. Nevertheless, JZ maintained the highest particle pH on dust days because it had the lowest particle acidity and the strongest buffering capacity on clean days. XX showed the smallest increase in particle pH, possibly because of the relatively weak contribution of alkaline cation input. Overall, the increase in particle pH during this dust episode was mainly driven by alkaline cations such as Ca^{2+}, while intercity differences in pH resulted from the combined effects of long-range dust transport and differences in local inorganic chemical composition.

https://doi.org/10.5194/egusphere-2026-3573
Preprint. Discussion started: 20 July 2026

3.4 The role of particle pH in secondary aerosol formation

Previous studies have shown that aqueous-phase reactions are a major pathway for sulfate formation in the North China region (Tao et al., 2020; Cai et al., 2024). In this study, sulfate formation rates through pH-dependent aqueous-phase pathways, including O_3 oxidation, TMI-catalyzed oxidation, and NO_2 oxidation of S(IV), were calculated for clean and dust days. The mean particle pH values for each city under clean and dust conditions are also marked in the figure. The results showed that TMI-catalyzed oxidation was consistently the dominant sulfate formation pathway under both clean and dust conditions. Its formation rates ranged from 2.5×10^{-1} to 2.0×10^{0} μg m^{-3} h^{-1} on clean days and from 1.3×10^{-2} to 5.0×10^{-1} μg m^{-3} h^{-1} on dust days, much higher than those of the O_3 and NO_2 oxidation pathways. Compared with clean days, the TMI-catalyzed sulfate formation rates decreased markedly in all cities as particle pH increased during the dust episode, with decreases of approximately 2.2×10^{-2}–1.5×10^{0} μg m^{-3} h^{-1}, corresponding to reductions of 75.2%–97.1%. The decreases were particularly large in JZ, ZZ, and SMX, reaching 97.1%, 93.8%, and 93.3%, respectively. This may be attributed to the decrease in Fe(III) and Mn(II) concentrations at higher pH, which reduced the TMI-catalyzed reaction rate.

In contrast, the reaction rates of the O_3 and NO_2 oxidation pathways were higher on dust days than on clean days in all cities. The O_3 oxidation rate increased from 2.5×10^{-7}–2.9×10^{-6} μg m^{-3} h^{-1} on clean days to 3.2×10^{-6}–6.7×10^{-5} μg m^{-3} h^{-1} on dust days. The NO_2 oxidation rate increased from 6.2×10^{-7}–6.3×10^{-6} μg m^{-3} h^{-1} to 2.1×10^{-6}–2.5×10^{-5} μg m^{-3} h^{-1}. These results indicate that the increase in particle pH during the dust episode favored sulfate formation through O_3 and NO_2 oxidation. However, because the TMI-catalyzed oxidation rate was much higher than those of the O_3 and NO_2

https://doi.org/10.5194/egusphere-2026-3573
Preprint. Discussion started: 20 July 2026

pathways, the increases in the O_3 and NO_2 oxidation rates were insufficient to offset the decrease in TMI-catalyzed oxidation. As a result, the overall aqueous-phase sulfate formation rate decreased in all cities. This result is generally consistent with the lower SOR values observed on dust days. This indicates that although dust transport increased particle pH, the higher-pH conditions suppressed TMI-catalyzed oxidation and reduced the efficiency of aqueous-phase sulfate formation.

The $\varepsilon(NO_3^-)$ values in the seven cities of central China were already high on clean days, ranging from 0.81 to 0.95, with the highest value in PY and the lowest in SQ. This indicates that nitrate gas-particle partitioning was dominated by the particle phase even during non-dust periods. During the dust episode, particle pH increased markedly in all cities, accompanied by a decrease in particle acidity, and $\varepsilon(NO_3^-)$ increased with increasing particle pH. The most pronounced increase was observed in SQ, where $\varepsilon(NO_3^-)$ increased from 0.81 to 0.95. ZZ and SMX also showed clear increases, from 0.88 to 0.97 and from 0.92 to 0.98, respectively. In contrast, the increases in PY, JZ, XX, and AY were relatively small. Notably, the increase in $\varepsilon(NO_3^-)$ during the dust episode was not fully consistent with the increase in particle pH among cities. Although JZ showed the largest increase in particle pH, its $\varepsilon(NO_3^-)$ increased only from 0.94 to 0.99, with an increase of approximately 0.05. By contrast, SQ exhibited a more pronounced increases in $\varepsilon(NO_3^-)$, with an increase of 0.14. This difference was mainly related to the response regime of $\varepsilon(NO_3^-)$ corresponding to the clean-day pH. When the clean-day pH was lower and located within the rapid-increase range of $\varepsilon(NO_3^-)$, the dust-induced increase in pH more effectively promoted nitrate partitioning into the particle phase, thereby enhancing the formation and accumulation of particulate nitrate.

https://doi.org/10.5194/egusphere-2026-3573
Preprint. Discussion started: 20 July 2026

4 Conclusions

The regional dust episode markedly altered $PM_{2.5}$ composition across the seven cities in central China. The mean contribution of CM to $PM_{2.5}$ increased to 53.2% on dust days. This contribution exceeded the 45.6% reported for Beijing in April 2023 but remained below the 69% observed during dust storms in the Horqin source region. Although the relative contribution of secondary inorganic aerosols decreased, substantial nitrate and sulfate formation persisted during the episode. Beyond these compositional changes, ISORROPIA-II simulations showed that particle pH increased in all cities, primarily because of enhanced inputs of Ca^{2+}, Mg^{2+}, and other non-volatile cations. During the dust episode, particle pH across the seven cities ranged from approximately 4.24 to 4.94. This range is broadly consistent with previously calculated values for Henan (4.5–5.2) and is also close to the values simulated over the southern North China Plain (4.4–5.7). Moreover, substantial intercity differences in particle pH remained and were primarily governed by local inorganic composition and acid–base buffering capacity. Transition-metal-ion-catalyzed oxidation remained the dominant aqueous-phase sulfate formation pathway, but its rate decreased by 75.2%–97.1% as particle pH increased. Although higher pH enhanced the O_3 and NO_2 oxidation pathways, these increases were insufficient to offset the decrease in the dominant TMI-catalyzed pathway. In contrast, the increase in particle pH promoted the partitioning of gaseous HNO_3 into the particle phase. In particular, for cities with relatively low clean-day pH located within the rapid-increase range of $\varepsilon(NO_3^-)$, even a pH increase that was not the largest among the cities could lead to rapid particulate nitrate accumulation.

These findings should nevertheless be interpreted in light of several uncertainties associated with

https://doi.org/10.5194/egusphere-2026-3573
Preprint. Discussion started: 20 July 2026

the pathway calculations and thermodynamic modeling. In the absence of H_2O_2 observations, the H_2O_2 oxidation pathway was not included in the calculation, which may have resulted in an underestimation of the total aqueous-phase sulfate production rate under moderately acidic conditions. For the TMI-catalyzed oxidation pathway, Fe(III) and Mn(II) concentrations were estimated using fixed solubility products at 298 K and pH-dependent precipitation equilibria. Because ionic-strength effects were not considered, the calculated reaction rates also remain uncertain. In addition, because forward-mode ISORROPIA-II calculations are based on thermodynamic equilibrium and require complete gas- and particle-phase inputs, the modeled particle pH and ALWC are also subject to uncertainty. Future studies should therefore conduct simultaneous measurements of H_2O_2 and key gas-phase species to strengthen the quantitative constraints on sulfate formation pathways and particle acidity.

Currently, nitrate has become a major challenge for regional $PM_{2.5}$ control. Its formation is regulated not only by precursor emissions such as NO_x, but also by particle acidity. Dust-derived CM not only increase $PM_{2.5}$ mass as particulate components, but also modify nitrate gas-particle partitioning by increasing particle pH, thereby favoring particulate nitrate accumulation. Therefore, future nitrate control strategies should continue to prioritize NO_x emission reductions while also considering the long-term management of crustal material and fugitive dust sources, particularly in regions frequently affected by dust episodes or characterized by substantial local dust contributions.

Data availability

All data in this work are available by contacting the corresponding authors, Xiaohui Bi and

https://doi.org/10.5194/egusphere-2026-3573
Preprint. Discussion started: 20 July 2026

Shenbo Wang (bixh@nankai.edu.cn and shbwang@zzu.edu.cn).

Supporting Information

The Supporting Information contains additional data, figures, and tables, some of which are referenced directly in the manuscript, as well as detailed descriptions of the field measurements and samples.

Author contributions

X.B. designed this study. H.Z. and S.W. analyzed the data and prepared the manuscript with the contributions of all coauthors. Y.Z. and Y.X. collected the data and contributed to the data analysis. Q.D. revised the paper. Y.F. provided funding acquisition and supervision. All authors have read and agreed to the published version of the manuscript.

Competing interests

The authors declare that they have no conflict of interest.

Acknowledgment

This work was supported by the General Program of the National Natural Science Foundation of China (No. 42275190). We thank Shujuan Shi for their contributions to the field observations.

https://doi.org/10.5194/egusphere-2026-3573
Preprint. Discussion started: 20 July 2026

Financial support

This work was supported by the General Program of the National Natural Science Foundation of China (No. 42275190).

References

Borjigin, A.; Bueh, C.; Yong, M.; Purevjav, G.; Xie, Z. Cross-border sand and dust storms between Mongolia and northern China in spring and their driving weather systems. Remote Sens., 16, 2164, https://doi.org/10.3390/rs16122164, 2024.

Cai, S.; Liu, T.; Huang, X.; Song, Y.; Wang, T.; Sun, Z.; Gao, J.; Ding, A. Important role of low cloud and fog in sulfate aerosol formation during winter haze over the North China Plain. Geophys. Res. Lett., 51, e2023GL106597, https://doi.org/10.1029/2023GL106597, 2024.

Chang, R. Y.-W.; Slowik, J. G.; Shantz, N. C.; Vlasenko, A.; Liggio, J.; Sjostedt, S. J.; Leaitch, W. R.; Abbatt, J. P. D. The hygroscopicity parameter (κ) of ambient organic aerosol at a field site subject to biogenic and anthropogenic influences: relationship to degree of aerosol oxidation. Atmos. Chem. Phys., 10, 5047–5064, https://doi.org/10.5194/acp-10-5047-2010, 2010.

Chen, S.; Jiang, N.; Huang, J.; Xu, X.; Zhang, H.; Zang, Z.; Huang, K.; Xu, X.; Wei, Y.; Guan, X.; Zhang, X.; Luo, Y.; Hu, Z.; Feng, T. Quantifying contributions of natural and anthropogenic dust emission from different climatic regions. Atmos. Environ., 191, 94–104, https://doi.org/10.1016/j.atmosenv.2018.07.043, 2018.

Chen, S.; Chen, J.; Zhang, Y.; Lin, J.; Bi, H.; Song, H.; Chen, Y.; Lian, L.; Liu, C.; Zhang, R. Anthropogenic dust: sources, characteristics and emissions. Environ. Res. Lett., 18, 103002, https://doi.org/10.1088/1748-9326/acf479, 2023.

Chen, S.; Zhao, D.; Huang, J.; He, J.; Chen, Y.; Chen, J.; Bi, H.; Lou, G.; Du, S.; Zhang, Y.; Yang, F. Mongolia contributed more than 42% of the dust concentrations in northern China in March and April 2023. Adv. Atmos. Sci., 40, 1549–1557, https://doi.org/10.1007/s00376-023-3062-1, 2023.

https://doi.org/10.5194/egusphere-2026-3573
Preprint. Discussion started: 20 July 2026

Chen, X.; Walker, J. T.; Geron, C. Chromatography related performance of the Monitor for AeRosols and GAses in ambient air (MARGA): laboratory and field-based evaluation. Atmos. Meas. Tech., 10, 3893–3908, https://doi.org/10.5194/amt-10-3893-2017, 2017.

Chen, Y.; Chen, S.; Bi, H.; Zhou, J.; Zhang, Y. Where is the dust source of 2023 several severe dust events in China? Bull. Am. Meteorol. Soc., 105, E2085–E2096, https://doi.org/10.1175/BAMS-D-23-0121.1, 2024.

Clegg, S. L.; Brimblecombe, P.; Wexler, A. S. Thermodynamic model of the system H^+-NH_4^+ - SO_4^{2-} - NO_3^- - H_2O at tropospheric temperatures. J. Phys. Chem. A, 102, 2137–2154, https://doi.org/10.1021/jp973042r, 1998.

Després, V. R.; Huffman, J. A.; Burrows, S. M.; Hoose, C.; Safatov, A. S.; Buryak, G.; Fröhlich-Nowoisky, J.; Elbert, W.; Andreae, M. O.; Pöschl, U.; Jaenicke, R. Primary biological aerosol particles in the atmosphere: a review. Tellus B, 64, 15598, https://doi.org/10.3402/tellusb.v64i0.15598, 2012.

Ding, J.; Zhao, P.; Su, J.; Dong, Q.; Du, X.; Zhang, Y. Aerosol pH and its driving factors in Beijing. Atmos. Chem. Phys., 19, 7939–7954, https://doi.org/10.5194/acp-19-7939-2019, 2019.

Dong, Z.; Su, F.; Zhang, Z.; Wang, S. Observation of chemical components of $PM_{2.5}$ and secondary inorganic aerosol formation during haze and sandy haze days in Zhengzhou, China. J. Environ. Sci., 88, 316–325, https://doi.org/10.1016/j.jes.2019.09.016, 2020.

Fountoukis, C.; Nenes, A. ISORROPIA II: a computationally efficient thermodynamic equilibrium model for K^+ - Ca^{2+} - Mg^{2+} - NH_4^+ - Na^+ - SO_4^{2-} - NO_3^- - Cl^- - H_2O aerosols. Atmos. Chem. Phys., 7, 4639–4659, https://doi.org/10.5194/acp-7-4639-2007, 2007.

Guo, H.; Xu, L.; Bougiatioti, A.; Cerully, K. M.; Capps, S. L.; Hite, J. R., Jr.; Carlton, A. G.; Lee, S.-H.; Bergin, M. H.; Ng, N. L.; Nenes, A.; Weber, R. J. Fine-particle water and pH in the southeastern United States. Atmos. Chem. Phys., 15, 5211–5228, https://doi.org/10.5194/acp-15-5211-2015, 2015.

Guo, H.; Sullivan, A. P.; Campuzano-Jost, P.; Schroder, J. C.; Lopez-Hilfiker, F. D.; Dibb, J. E.; Jimenez, J. L.; Thornton, J. A.; Brown, S. S.; Nenes, A.; Weber, R. J. Fine particle pH and the

https://doi.org/10.5194/egusphere-2026-3573
Preprint. Discussion started: 20 July 2026

partitioning of nitric acid during winter in the northeastern United States. J. Geophys. Res. Atmos., 121, 10355–10376, https://doi.org/10.1002/2016JD025311, 2016.

Guo, H.; Otjes, R.; Schlag, P.; Kiendler-Scharr, A.; Nenes, A.; Weber, R. J. Effectiveness of ammonia reduction on control of fine particle nitrate. Atmos. Chem. Phys., 18, 12241–12256, https://doi.org/10.5194/acp-18-12241-2018, 2018.

Hrdina, A.; Murphy, J. G.; Hallar, A. G.; Lin, J. C.; Moravek, A.; Bares, R.; Petersen, R. C.; Franchin, A.; Middlebrook, A. M.; Goldberger, L.; Lee, B. H.; Baasandorj, M.; Brown, S. S. The role of coarse aerosol particles as a sink of HNO_3 in wintertime pollution events in the Salt Lake Valley. Atmos. Chem. Phys., 21, 8111–8126, https://doi.org/10.5194/acp-21-8111-2021, 2021.

Huo, Q.; Yin, Z.; Ma, X.; Wang, H. Distinctive dust weather intensities in North China resulted from two types of atmospheric circulation anomalies. Atmos. Chem. Phys., 25, 1711–1724, https://doi.org/10.5194/acp-25-1711-2025, 2025.

Itahashi, S.; Hattori, S.; Ito, A.; Sadanaga, Y.; Yoshida, N.; Matsuki, A. Role of dust and iron solubility in sulfate formation during the long-range transport in East Asia evidenced by ^{17}O-excess signatures. Environ. Sci. Technol., 56, 13634–13643, https://doi.org/10.1021/acs.est.2c03574, 2022.

Jia, X.; Gu, W.; Peng, C.; Li, R.; Chen, L.; Wang, H.; Wang, H.; Wang, X.; Tang, M. Heterogeneous reaction of $CaCO_3$ with NO_2 at different relative humidities: kinetics, mechanisms, and impacts on aerosol hygroscopicity. J. Geophys. Res. Atmos., 126, e2021JD034826, https://doi.org/10.1029/2021JD034826, 2021.

Karydis, V. A.; Tsimpidi, A. P.; Pozzer, A.; Lelieveld, J. How alkaline compounds control atmospheric aerosol particle acidity. Atmos. Chem. Phys., 21, 14983–15001, https://doi.org/10.5194/acp-21-14983-2021, 2021.

Lang, H.; Zhang, Y.; Zhong, S.; Rao, Y.; Zhou, M.; Qiu, J.; Li, J.; Liu, D.; Couvidat, F.; Favez, O.; Hauglustaine, D.; Ge, X. Dust pollution substantially weakens the impact of ammonia emission reduction on particulate nitrate formation. Atmos. Chem. Phys., 25, 10587–10601, https://doi.org/10.5194/acp-25-10587-2025, 2025.

https://doi.org/10.5194/egusphere-2026-3573
Preprint. Discussion started: 20 July 2026

Li, C.; Hu, Y.; Chen, J.; Ma, Z.; Ye, X.; Yang, X.; Wang, L.; Wang, X.; Mellouki, A. Physiochemical properties of carbonaceous aerosol from agricultural residue burning: density, volatility, and hygroscopicity. Atmos. Environ., 140, 94–105, https://doi.org/10.1016/j.atmosenv.2016.05.052, 2016.

Li, W.; Ito, A.; Wang, G.; Zhi, M.; Xu, L.; Yuan, Q.; Zhang, J.; Liu, L.; Wu, F.; Laskin, A.; Zhang, D.; Zhang, X.; Zhu, T.; Chen, J.; Mihalopoulos, N.; Bougiatioti, A.; Kanakidou, M.; Wang, G.; Hu, H.; Zhao, Y.; Shi, Z. Aqueous-phase secondary organic aerosol formation on mineral dust. Natl. Sci. Rev., 12, nwaf221, https://doi.org/10.1093/nsr/nwaf221, 2025.

Liu, Y.; Deng, Y.; Liu, J.; Fang, X.; Wang, T.; Li, K.; Gong, K.; Bacha, A. U.; Nabi, I.; Ge, Q.; Zhang, X.; George, C.; Zhang, L. A novel pathway of atmospheric sulfate formation through carbonate radicals. Atmos. Chem. Phys., 22, 9175–9197, https://doi.org/10.5194/acp-22-9175-2022, 2022.

Liu, Z.; Qi, J.; Ni, Y.; Xue, L.; Liu, X. Enhanced atmospheric oxidation and particle reductions driving changes to nitrate formation mechanisms across coastal and inland regions of North China. Atmos. Chem. Phys., 25, 8719–8742, https://doi.org/10.5194/acp-25-8719-2025, 2025.

Ma, P.; Quan, J.; Dou, Y.; Pan, Y.; Liao, Z.; Cheng, Z.; Jia, X.; Wang, Q.; Zhan, J.; Ma, W.; Zheng, F.; Wang, Y.; Zhang, Y.; Hua, C.; Yan, C.; Kulmala, M.; Liu, Y.; Huang, X.; Yuan, B.; Brown, S. S.; Liu, Y. Regime-dependence of nocturnal nitrate formation via N_2O_5 hydrolysis and its implication for mitigating nitrate pollution. Geophys. Res. Lett., 50, e2023GL106183, https://doi.org/10.1029/2023GL106183, 2023.

Mahowald, N.; Albani, S.; Kok, J. F.; Engelstaedter, S.; Scanza, R.; Ward, D. S.; Flanner, M. G. The size distribution of desert dust aerosols and its impact on the Earth system. Aeolian Res., 15, 53–71, https://doi.org/10.1016/j.aeolia.2013.09.002, 2014.

McKendry, I. G.; Strawbridge, K. B.; O'Neill, N. T.; Macdonald, A. M.; Liu, P. S. K.; Leaitch, W. R.; Anlauf, K. G.; Jaegle, L.; Fairlie, T. D.; Westphal, D. L. Trans-Pacific transport of Saharan dust to western North America: a case study. J. Geophys. Res. Atmos., 112, D01103, https://doi.org/10.1029/2006JD007129, 2007.

Milousis, A.; Klingmüller, K.; Tsimpidi, A. P.; Kok, J. F.; Kanakidou, M.; Nenes, A.; Karydis, V. A.

https://doi.org/10.5194/egusphere-2026-3573
Preprint. Discussion started: 20 July 2026

572 Impact of mineral dust on the global nitrate aerosol direct and indirect radiative effect. Atmos.
573 Chem. Phys., 25, 1333–1351, https://doi.org/10.5194/acp-25-1333-2025, 2025.
574 Nenes, A.; Pandis, S. N.; Weber, R. J.; Russell, A. Aerosol pH and liquid water content determine when
575 particulate matter is sensitive to ammonia and nitrate availability. Atmos. Chem. Phys., 20, 3249–
576 3258, https://doi.org/10.5194/acp-20-3249-2020, 2020.
577 Rumsey, I. C.; Cowen, K. A.; Walker, J. T.; Kelly, T. J.; Hanft, E. A.; Mishoe, K.; Rogers, C.; Proost,
578 R.; Beachley, G. M.; Lear, G.; Frelink, T.; Otjes, R. P. An assessment of the performance of the
579 Monitor for AeRosols and GAses in ambient air (MARGA): a semi-continuous method for
580 soluble compounds. Atmos. Chem. Phys., 14, 5639–5658, https://doi.org/10.5194/acp-14-5639-
581 2014, 2014.
582 Rumsey, I. C.; Walker, J. T. Application of an online ion-chromatography-based instrument for gradient
583 flux measurements of speciated nitrogen and sulfur. Atmos. Meas. Tech., 9, 2581–2592,
584 https://doi.org/10.5194/amt-9-2581-2016, 2016.
585 Pye, H. O. T.; Nenes, A.; Alexander, B.; Ault, A. P.; Barth, M. C.; Clegg, S. L.; Collett, J. L., Jr.; Fahey,
586 K. M.; Hennigan, C. J.; Herrmann, H.; Kanakidou, M.; Kelly, J. T.; Ku, I.-T.; McNeill, V. F.;
587 Riemer, N.; Schaefer, T.; Shi, G.; Tilgner, A.; Walker, J. T.; Wang, T.; Weber, R.; Xing, J.; Zaveri,
588 R. A.; Zuend, A. The acidity of atmospheric particles and clouds. Atmos. Chem. Phys., 20, 4809–
589 4888, https://doi.org/10.5194/acp-20-4809-2020, 2020.
590 Ryder, C. L.; Highwood, E. J.; Walser, A.; Seibert, P.; Philipp, A.; Weinzierl, B. Coarse and giant
591 particles are ubiquitous in Saharan dust export regions and are radiatively significant over the
592 Sahara. Atmos. Chem. Phys., 19, 15353–15376, https://doi.org/10.5194/acp-19-15353-2019,
593 2019.
594 Song, H.; Lu, K.; Ye, C.; Dong, H.; Li, S.; Chen, S.; Wu, Z.; Zheng, M.; Zeng, L.; Hu, M.; Zhang, Y.
595 A comprehensive observation-based multiphase chemical model analysis of sulfur dioxide
596 oxidations in both summer and winter. Atmos. Chem. Phys., 21, 13713–13727,
597 https://doi.org/10.5194/acp-21-13713-2021, 2021.
598 Tang, Y.; Han, S.; Yao, Q.; Cai, Z.; Qiu, Y.; Feng, J. Analysis of a severe regional haze-fog-dust episode

https://doi.org/10.5194/egusphere-2026-3573
Preprint. Discussion started: 20 July 2026

over North China in autumn by using multiple observation data. Aerosol Air Qual. Res., 20, 2211–2225, https://doi.org/10.4209/aaqr.2019.11.0567, 2020.

Tao, W.; Su, H.; Zheng, G.; Wang, J.; Wei, C.; Liu, L.; Ma, N.; Li, M.; Zhang, Q.; Pöschl, U.; Cheng, Y. Aerosol pH and chemical regimes of sulfate formation in aerosol water during winter haze in the North China Plain. Atmos. Chem. Phys., 20, 11729–11746, https://doi.org/10.5194/acp-20-11729-2020, 2020.

Textor, C.; Schulz, M.; Guibert, S.; Kinne, S.; Balkanski, Y.; Bauer, S.; Berntsen, T.; Berglen, T.; Boucher, O.; Chin, M.; Dentener, F.; Diehl, T.; Easter, R.; Feichter, H.; Fillmore, D.; Ghan, S.; Ginoux, P.; Gong, S.; Grini, A.; Hendricks, J.; Horowitz, L.; Huang, P.; Isaksen, I.; Iversen, I.; Kloster, S.; Koch, D.; Kirkevåg, A.; Kristjansson, J. E.; Krol, M.; Lauer, A.; Lamarque, J. F.; Liu, X.; Montanaro, V.; Myhre, G.; Penner, J.; Pitari, G.; Reddy, S.; Seland, Ø.; Stier, P.; Takemura, T.; Tie, X. Analysis and quantification of the diversities of aerosol life cycles within AeroCom. Atmos. Chem. Phys., 6, 1777–1813, https://doi.org/10.5194/acp-6-1777-2006, 2006.

Tian, Y.; Chen, G.; Wang, H.; Huang-Fu, Y.; Shi, G.; Han, B.; Feng, Y. Source regional contributions to $PM_{2.5}$ in a megacity in China using an advanced source regional apportionment method. Chemosphere, 147, 256–263, https://doi.org/10.1016/j.chemosphere.2015.12.132, 2016.

Tilgner, A.; Schaefer, T.; Alexander, B.; Barth, M.; Collett, J. L., Jr.; Fahey, K. M.; Nenes, A.; Pye, H. O. T.; Herrmann, H.; McNeill, V. F. Acidity and the multiphase chemistry of atmospheric aqueous particles and clouds. Atmos. Chem. Phys., 21, 13483–13536, https://doi.org/10.5194/acp-21-13483-2021, 2021.

Trebs, I.; Meixner, F. X.; Slanina, J.; Otjes, R.; Jongejan, P.; Andreae, M. O. Real-time measurements of ammonia, acidic trace gases and water-soluble inorganic aerosol species at a rural site in the Amazon Basin. Atmos. Chem. Phys., 4, 967–987, https://doi.org/10.5194/acp-4-967-2004, 2004.

Vasilakos, P.; Russell, A.; Weber, R.; Nenes, A. Understanding nitrate formation in a world with less sulfate. Atmos. Chem. Phys., 18, 12765–12775, https://doi.org/10.5194/acp-18-12765-2018, 2018.

Wang, S.; Wang, L.; Li, Y.; Wang, C.; Wang, W.; Yin, S.; Zhang, R. Effect of ammonia on fine-particle

https://doi.org/10.5194/egusphere-2026-3573
Preprint. Discussion started: 20 July 2026

626 pH in agricultural regions of China: comparison between urban and rural sites. Atmos. Chem.
627 Phys., 20, 2719–2734, https://doi.org/10.5194/acp-20-2719-2020, 2020.
628 Wang, S.; Wang, L.; Wang, N.; Ma, S.; Su, F.; Zhang, R. Formation of droplet-mode second
629 ary inorganic aerosol dominated the increased $PM_{2.5}$ during both local and transport haze
630 episodes in Zhengzhou, China. Chemosphere, 269, 128744, https://doi.org/10.1016/j.chem
631 osphere.2020.128744, 2021.
632 Wang, S.; Wang, L.; Fan, X.; Wang, N.; Ma, S.; Zhang, R. Formation pathway of secondary inorganic
633 aerosol and its influencing factors in northern China: comparison between urban and rural sites.
634 Sci. Total Environ., 840, 156404, https://doi.org/10.1016/j.scitotenv.2022.156404, 2022.
635 Wang, S.; Wang, L.; Fan, X.; Wang, N.; Ma, S.; Zhang, R. Differences in $PM_{2.5}$ components between
636 urban and rural sites during a heavy haze event in northern Henan Province. Huan Jing Ke Xue,
637 44, 11–19, https://doi.org/10.13227/j.hjkx.202203047, 2023.
638 Wang, T.; Liu, M.; Liu, M.; Song, Y.; Xu, Z.; Shang, F.; Huang, X.; Liao, W.; Wang, W.;
639 Ge, M.; Cao, J.; Hu, J.; Tang, G.; Pan, Y.; Hu, M.; Zhu, T. Sulfate formation apportion
640 ment during winter haze events in North China. Environ. Sci. Technol., 56, 7771–7778,
641 https://doi.org/10.1021/acs.est.2c02533, 2022.
642 Wang, W.; Liu, M.; Wang, T.; Song, Y.; Zhou, L.; Cao, J.; Hu, J.; Tang, G.; Chen, Z.; Li, Z.; Xu, Z.;
643 Peng, C.; Lian, C.; Chen, Y.; Pan, Y.; Zhang, Y.; Sun, Y.; Li, W.; Zhu, T.; Tian, H.; Ge, M. Sulfate
644 formation is dominated by manganese-catalyzed oxidation of SO_2 on aerosol surfaces during haze
645 events. Nat. Commun., 12, 1993, https://doi.org/10.1038/s41467-021-22091-6, 2021.
646 Wei, J.; Hou, T.; Li, Z.; Guo, S.; Li, Z. Changes in chemical composition, sources, and health risk of
647 $PM_{2.5}$ with sand storm at a small city in North China. Aerosol Air Qual. Res., 22, 220114,
648 https://doi.org/10.4209/aaqr.220114, 2022.
649 Wei, J.; Li, Z.; Chen, X.; Li, C.; Sun, Y.; Wang, J.; Lyapustin, A.; Brasseur, G. P.; Jiang, M.; Sun, L.;
650 Wang, T.; Jung, C. H.; Qiu, B.; Fang, C.; Liu, X.; Hao, J.; Wang, Y.; Zhan, M.; Song, X.; Liu, Y.
651 Separating daily 1 km $PM_{2.5}$ inorganic chemical composition in China since 2000 via deep
652 learning integrating ground, satellite, and model data. Environ. Sci. Technol., 57, 18282–18295,

https://doi.org/10.5194/egusphere-2026-3573
Preprint. Discussion started: 20 July 2026

https://doi.org/10.1021/acs.est.3c00272, 2023.

Wu, F.; Kong, S.; Yan, Q.; Wang, W.; Liu, H.; Wu, J.; Zheng, H.; Zheng, S.; Cheng, Y.; Niu, Z.; Liu, D.; Qi, S. Sub-type source profiles of fine particles for fugitive dust and accumulative health risks of heavy metals: a case study in a fast-developing city of China. Environ. Sci. Pollut. Res., 27, 16554–16573, https://doi.org/10.1007/s11356-020-08136-1, 2020.

Yan, C.; Tham, Y. J.; Zha, Q.; Wang, X.; Xue, L.; Dai, J.; Wang, Z.; Wang, T. Fast heterog eneous loss of N_2O_5 leads to significant nighttime NO_x removal and nitrate aerosol form ation at a coastal background environment of southern China. Sci. Total Environ., 677, 637–647, https://doi.org/10.1016/j.scitotenv.2019.04.389, 2019.

Zhang, B.; Shen, H.; Liu, P.; Guo, H.; Hu, Y.; Chen, Y.; Xie, S.; Xi, Z.; Skipper, T. N.; Russell, A. G. Significant contrasts in aerosol acidity between China and the United States. Atmos. Chem. Phys., 21, 8341–8356, https://doi.org/10.5194/acp-21-8341-2021, 2021.

Zhang, S.; Li, D.; Ge, S.; Wu, C.; Xu, X.; Liu, X.; Li, R.; Zhang, F.; Wang, G. Elucidating the mechanism on the transition-metal ion-synergetic-catalyzed oxidation of SO_2 with implications for sulfate formation in Beijing haze. Environ. Sci. Technol., 58, 2912–2921, https://doi.org/10.1021/acs.est.3c08411, 2024.

Zhang, X.; Wang, L.; Wang, N.; Ma, S.; Wang, S.; Zhang, R.; Zhang, D.; Wang, M.; Zhang, H. Measurement report: elevated atmospheric ammonia may promote particle pH and HONO formation—insights from the COVID-19 pandemic. Atmos. Chem. Phys., 24, 9885–9898, https://doi.org/10.5194/acp-24-9885-2024, 2024.

Zhang, Y.; Li, N.; Tang, K.; Wang, M.; Li, H.; Li, K.; Zheng, B.; Zhang, Q.; Gao, M.; Fang, J.; Zhang, H.; Cui, S.; Wang, J.; Chen, M.; Liao, H.; Ge, X.; Hauglustaine, D.; Balkanski, Y.; Ciais, P.; Jiang, G. Widespread surface ozone reduction triggered by dust storm disturbance on ozone production and destruction chemistry. Sci. Adv., 11, eadr4297, https://doi.org/10.1126/sciadv.adr4297, 2025.

Zhang, Z.; Kuang, Z.; Yu, C.; Wu, D.; Shi, Q.; Zhang, S.; Wang, Z.; Liu, D. Trans-boundary dust transport of dust storms in northern China: a study utilizing ground-based lidar network and CALIPSO satellite. Remote Sens., 16, 1196, https://doi.org/10.3390/rs16071196, 2024.

https://doi.org/10.5194/egusphere-2026-3573
Preprint. Discussion started: 20 July 2026

680 Zhao, X.; Zhao, X.; Liu, P.; Chen, D.; Zhang, C.; Xue, C.; Liu, J.; Xu, J.; Mu, Y. Transport pathways
681 of nitrate formed from nocturnal N_2O_5 hydrolysis aloft to the ground level in winter North China
682 Plain. Environ. Sci. Technol., 57, 2715–2725, https://doi.org/10.1021/acs.est.3c00086, 2023.
683 Zheng, B.; Zhang, Q.; Zhang, Y.; He, K. B.; Wang, K.; Zheng, G. J.; Duan, F. K.; Ma, Y. L.; Kimoto,
684 T. Heterogeneous chemistry: a mechanism missing in current models to explain secondary
685 inorganic aerosol formation during the January 2013 haze episode in North China. Atmos. Chem.
686 Phys., 15, 2031–2049, https://doi.org/10.5194/acp-15-2031-2015, 2015.
687 Zhou, M.; Zheng, G.; Wang, H.; Qiao, L.; Zhu, S.; Huang, D.; An, J.; Lou, S.; Tao, S.; Wang, Q.; Yan,
688 R.; Ma, Y.; Chen, C.; Cheng, Y.; Su, H.; Huang, C. Long-term trends and drivers of aerosol pH in
689 eastern China. Atmos. Chem. Phys., 22, 13833–13844, https://doi.org/10.5194/acp-22-13833-
690 2022, 2022.
691

https://doi.org/10.5194/egusphere-2026-3573
Preprint. Discussion started: 20 July 2026

692 **Figures**

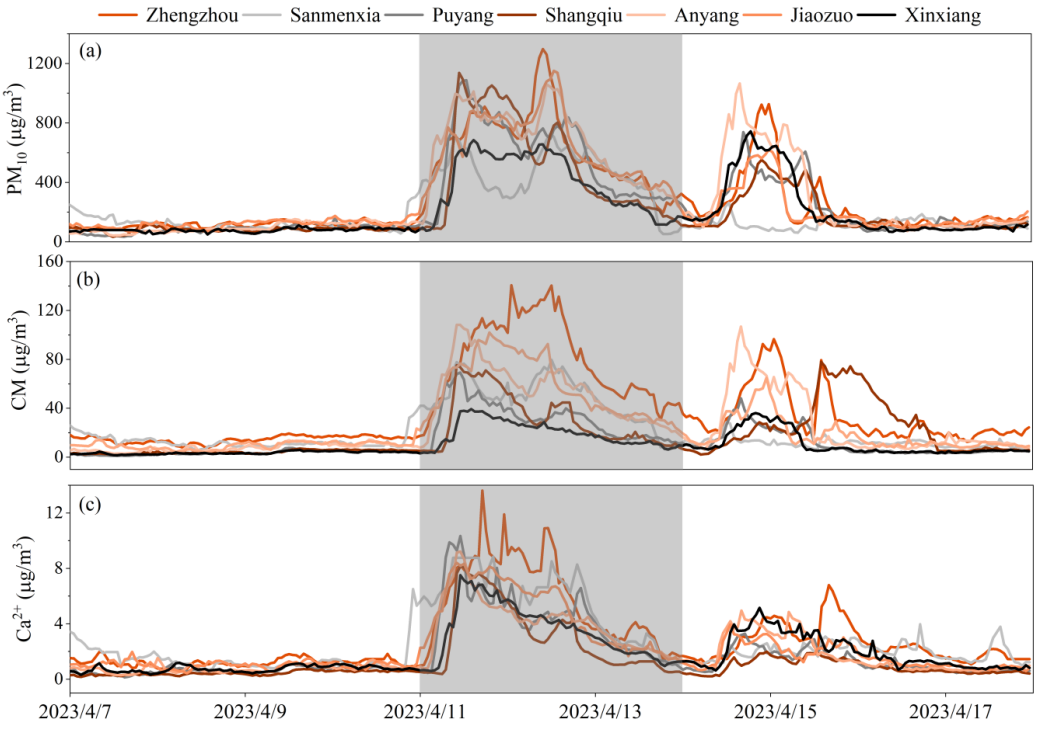

693

694 Figure 1. Time series of PM_{10}, crustal material (CM), and Ca^{2+} concentrations across seven cities in
695 central China during the observation period. The shaded area denotes the dust pollution episode.

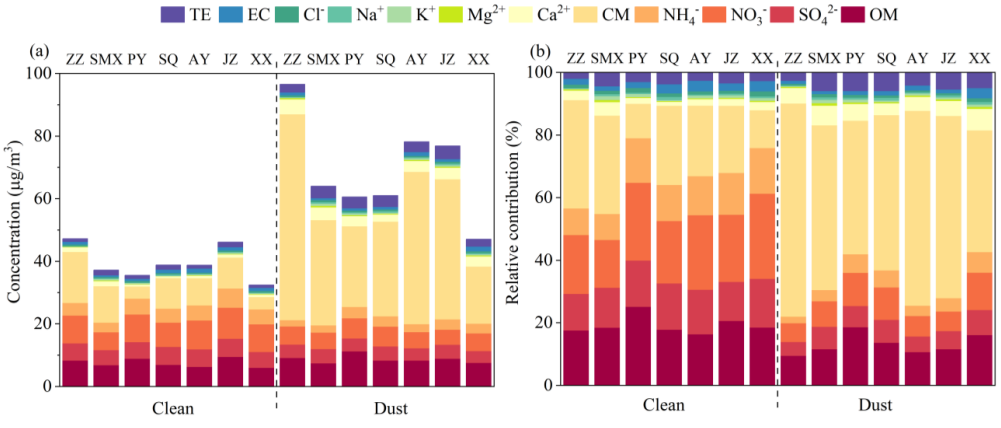

696

697 Figure 2. Chemical composition of $PM_{2.5}$ across seven cities in central China. (a) mass concentrations
698 of individual components; (b) mass fractions of individual components in $PM_{2.5}$.

https://doi.org/10.5194/egusphere-2026-3573
Preprint. Discussion started: 20 July 2026

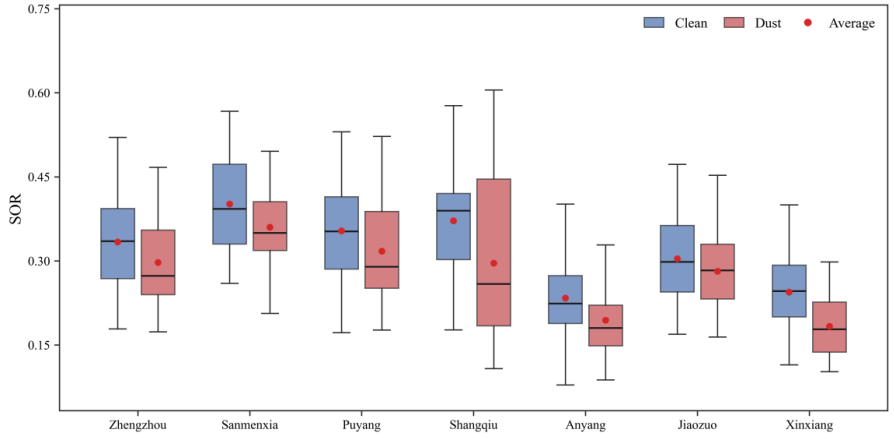

Figure 3. Box-and-whisker plots of SOR in each city on clean and dust days. Red dots and black horizontal lines denote the mean and median, respectively. The boxes span the 25th–75th percentiles, with the central line indicating the median, while the lower and upper whiskers represent the 10th and 90th percentiles, respectively.

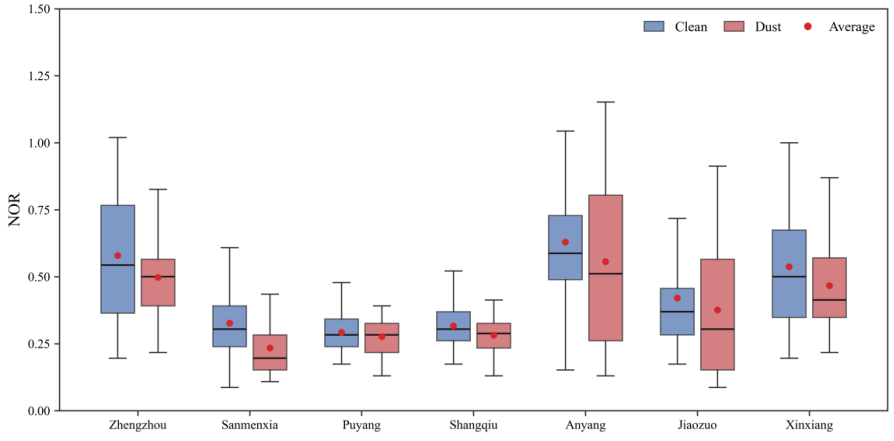

Figure 4. Box-and-whisker plots of NOR in each city on clean and dust days. Red dots and black horizontal lines denote the mean and median, respectively. The boxes span the 25th–75th percentiles, with the central line indicating the median, while the lower and upper whiskers represent the 10th and 90th percentiles, respectively.

https://doi.org/10.5194/egusphere-2026-3573
Preprint. Discussion started: 20 July 2026

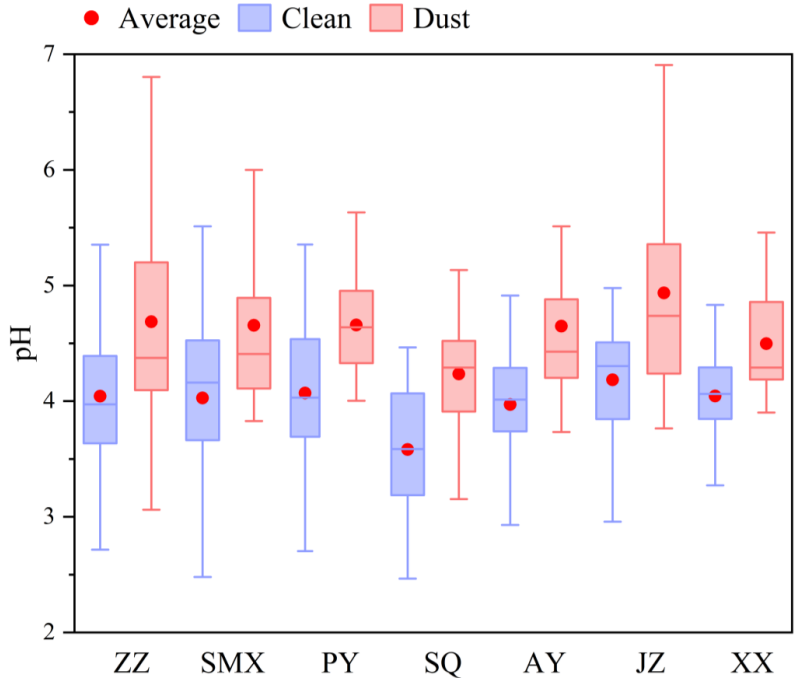

Figure 5. Box-and-whisker plots of particle pH across seven cities in central China during clean and dust-polluted periods. Red dots denote the mean values, while the blue and red horizontal lines indicate the median values for clean and dust-polluted periods, respectively. The boxes span the 25th–75th percentiles, while the lower and upper whiskers represent the 10th and 90th percentiles, respectively.

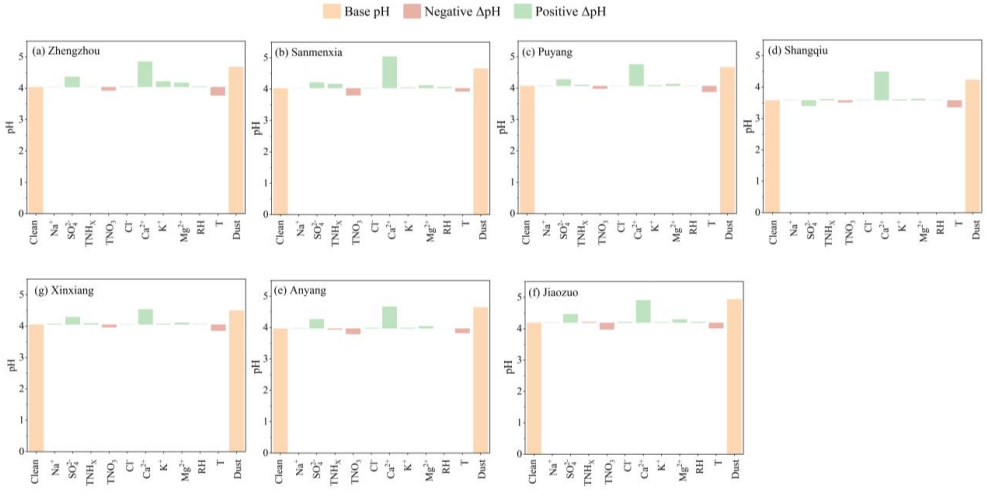

Figure 6. Factors driving particle pH variations during the dust episode in Zhengzhou (a), Sanmenxia

https://doi.org/10.5194/egusphere-2026-3573
Preprint. Discussion started: 20 July 2026

(b), Puyang (c), Shangqiu (d), Anyang (e), Jiaozuo (f), and Xinxiang (g). TNH_x represents NH_4^+ and NH_3, and TNO_3 represents NO_3^-.

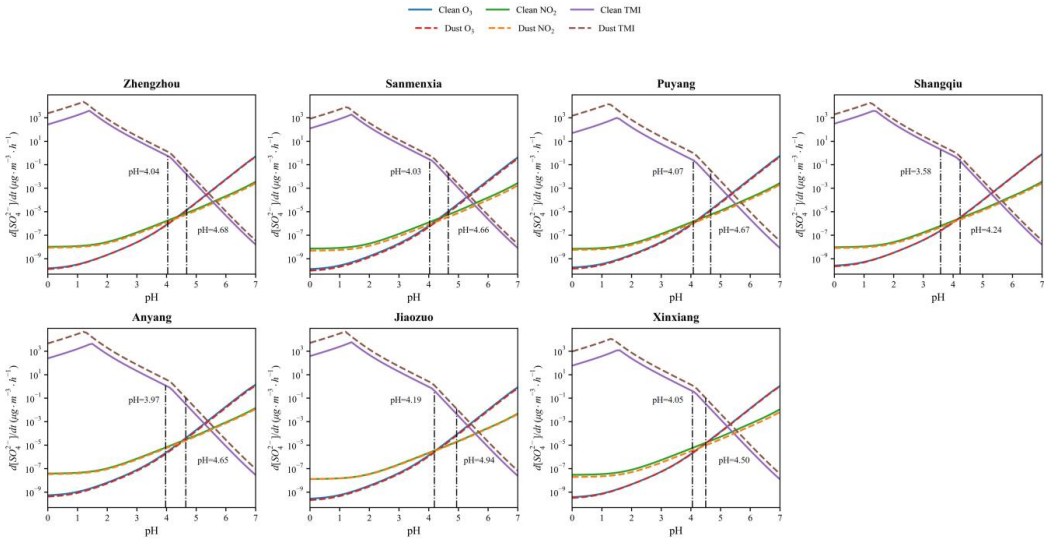

Figure 7. Calculated sulfate production rates through individual aqueous-phase reaction pathways as a function of particle pH across seven cities in central China under clean and dust conditions. Solid and dashed curves represent clean and dust days, respectively. The left and right vertical lines indicate the city-specific mean particle pH values on clean and dust days, respectively.

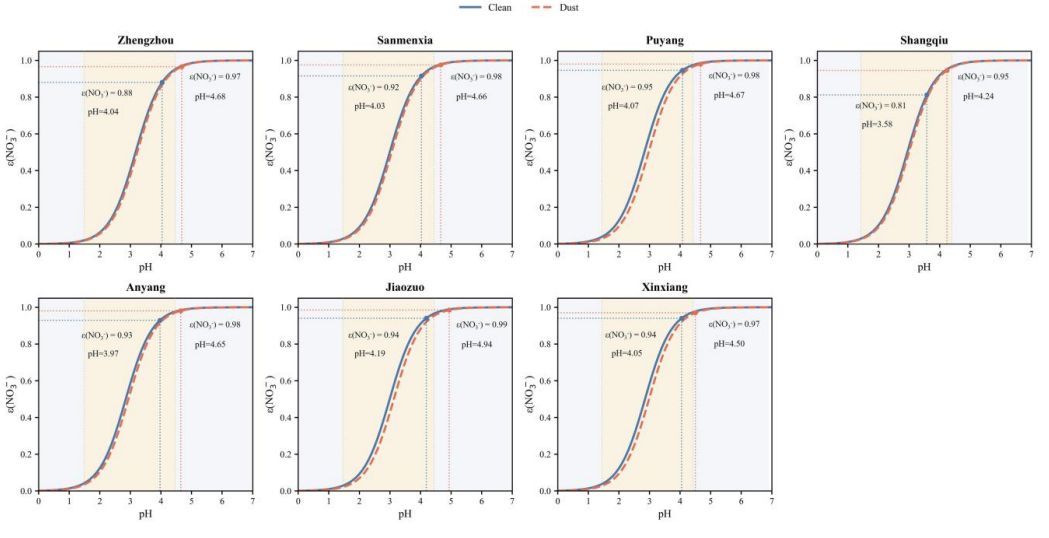

Figure 8. Variation in the particle-phase nitrate fraction, $\varepsilon(NO_3^-)$, with particle pH across seven cities in

https://doi.org/10.5194/egusphere-2026-3573
Preprint. Discussion started: 20 July 2026

central China. Solid and dashed curves represent clean and dust days, respectively. The blue and orange vertical lines indicate the city-specific mean particle pH values on clean and dust days, respectively, while the corresponding horizontal dotted lines indicate the $\varepsilon(NO_3^-)$ values at these pH levels. The yellow-shaded region denotes the pH range over which $\varepsilon(NO_3^-)$ increases rapidly, whereas the blue-shaded regions on either side indicate ranges characterized by slower increases in $\varepsilon(NO_3^-)$.

https://doi.org/10.5194/egusphere-2026-3573
Preprint. Discussion started: 20 July 2026

732 **Table**

733 Table 1. Average pollutant concentrations across seven cities in central China during clean and dust
734 periods (μg/m^3).

Cities	Substances	Clean	Dust
Zhengzhou	PM_{10}	120.6 ± 20.5	510.5 ± 282.8
	$PM_{2.5}$	52.1 ± 14.3	134.5 ± 77.0
	CM	16.4 ± 4.0	65.8 ± 34.3
	Ca^{2+}	1.4 ± 0.5	4.8 ± 2.9
Sanmenxia	PM_{10}	119.2 ± 41.9	313.1 ± 209.5
	$PM_{2.5}$	42.4 ± 10.4	97.6 ± 63.5
	CM	11.7 ± 4.7	33.7 ± 22.3
	Ca^{2+}	1.6 ± 0.9	4.0 ± 2.5
Puyang	PM_{10}	92.7 ± 26.5	470.0 ± 259.3
	$PM_{2.5}$	28.7 ± 8.0	81.8 ± 34.2
	CM	3.9 ± 1.6	25.8 ± 15.3
	Ca^{2+}	0.7 ± 0.2	3.3 ± 2.3
Shangqiu	PM_{10}	91.5 ± 20.4	414.5 ± 299.8
	$PM_{2.5}$	40.6 ± 14.8	106.5 ± 57.4
	CM	9.8 ± 13.8	30.3 ± 22.6
	Ca^{2+}	0.5 ± 0.2	2.3 ± 2.1
Anyang	PM_{10}	101.6 ± 28.9	576.1 ± 288.3
	$PM_{2.5}$	35.6 ± 11.1	123.1 ± 56.8
	CM	8.8 ± 3.2	48.7 ± 27.3
	Ca^{2+}	0.8 ± 0.2	3.5 ± 1.8
Jiaozuo	PM_{10}	123.0 ± 26.9	493.0 ± 272.6
	$PM_{2.5}$	50.2 ± 15.6	125.3 ± 55.1
	CM	9.9 ± 2.7	44.8 ± 26.3
	Ca^{2+}	1.0 ± 0.3	3.7 ± 2.3
Xinxiang	PM_{10}	81.9 ± 13.2	377.4 ± 206.0
	$PM_{2.5}$	38.5 ± 10.8	104.3 ± 51.4
	CM	3.9 ± 1.1	18.3 ± 10.6
	Ca^{2+}	0.9 ± 0.4	3.2 ± 1.7

735